J. Fluid Mech. (2017), *vol.* 812, *pp.* 841–865.
doi:10.1017/jfm.2016.830

Elastic deformations driven by non-uniform lubrication flows

Shimon Rubin[1], Arie Tulchinsky[1], Amir D. Gat[1,†] and Moran Bercovici[1,†]

[1]Faculty of Mechanical Engineering, Technion – Israel Institute of Technology, Haifa, Israel

(Received 23 May 2016; revised 30 November 2016; accepted 5 December 2016;
first published online 5 January 2017)

The ability to create dynamic deformations of micron-sized structures is relevant to a wide variety of applications such as adaptable optics, soft robotics and reconfigurable microfluidic devices. In this work, we examine non-uniform lubrication flow as a mechanism to create complex deformation fields in an elastic plate. We consider a Kirchhoff–Love elasticity model for the plate and Hele-Shaw flow in a narrow gap between the plate and a parallel rigid surface. Based on linearization of the Reynolds equation, we obtain a governing equation which relates elastic deformations to gradients in non-homogeneous physical properties of the fluid (e.g. body forces, viscosity and slip velocity). We then focus on a specific case of non-uniform Helmholtz–Smoluchowski electro-osmotic slip velocity, and provide a method for determining the zeta-potential distribution necessary to generate arbitrary static and quasi-static deformations of the elastic plate. Extending the problem to time-dependent solutions, we analyse transient effects on asymptotically static solutions, and finally provide a closed form solution for a Green's function for time periodic actuations.

Key words: fluid–structure interactions, Hele-Shaw flows, microfluidics

1. Introduction

Microstructures that can be dynamically deformed to desired patterns may hold promise for new applications in various fields such as adaptable optics, soft robotics and reconfigurable microfluidics (Unger *et al.* 2000; Chronis *et al.* 2003; Trivedi *et al.* 2008). In this work, we suggest the achievement of such dynamic deformations by the use of non-uniform lubrication flows in a narrow gap between two plates (Hele-Shaw flow) in which at least one of the plates is elastic, and the pressure in the fluid is used to exert forces on the plate.

Lubrication flows in the gap between an elastic plate and a rigid surface have been previously studied in the context of Taylor–Saffman instability (Pihler-Puzović *et al.* 2012; Al-Housseiny, Christov & Stone 2013), viscous peeling (Hosoi & Mahadevan 2004; Lister, Peng & Neufeld 2013), deformation due to injection of a fluid (Peng *et al.* 2015; Pihler-Puzović *et al.* 2015) and forced motion of an elastic plate pinned at one end (Trinh, Wilson & Stone 2014). Common to previous works is that the

† Email addresses for correspondence: amirgat@tx.technion.ac.il, mberco@technion.ac.il

deformations are realized by applying pressure or force at the outer edges of the cell, and thus allow only a limited set of elastic deformations to be achieved.

More complex pressure distributions can be achieved by using non-homogeneities of surface properties such as electro-osmotic slip velocity, and slip length over superhydrophobic surfaces. For example, Ajdari (1995, 1996) considered two-dimensional electro-osmotic flow (EOF) and demonstrated that undulation of a rigid plate on top of another plate having periodic distribution of zeta potential breaks left/right symmetry and gives rise to net flow generation between the plates. Feuillebois, Bazant & Vinogradova (2009) derived rigorous bounds on the effective slip of two-component textures in thin channels, which can guide the design of superhydrophobic surfaces for micro/nanofluidics. Recently, Boyko *et al.* (2015) considered properties of non-uniform and depth-averaged EOF in a Hele-Shaw cell due to local zeta-potential distributions, and determined the necessary zeta-potential distributions to generate complex flow patterns. To the best of our knowledge, all non-uniform flow studies have been performed between rigid plates.

The aim of this work is to examine the utilization of pressure gradients, formed due to non-uniform fluid properties in elastic Hele-Shaw configurations, as a mechanism to create desired dynamic deformations. The paper is structured as follows. In § 2, we combine low Reynolds number and shallow geometry assumptions (lubrication approximation) with a Kirchhoff–Love elastic model, to derive the governing equation for an elastic plate in a small deformation limit, driven by spatial gradients in the fluid properties. In § 3, we consider the limiting case of rigid walls and provide matching conditions for the pressure and stream function across piecewise constant non-homogeneity, and then utilize them to obtain the resulting pressure for the case of axially symmetric non-homogeneities. We then focus on a specific case where the non-homogeneity is constituted by non-uniform EOF (i.e. non-uniform Helmholtz–Smoluchowski slip velocity) as an actuation mechanism, and in § 4 obtain an analytical expression for the Helmholtz–Smoluchowski slip velocity distribution necessary to generate small but otherwise arbitrary static deformations. In § 5, we determine the necessary Helmholtz–Smoluchowski velocity distribution to actuate arbitrary asymptotically static time-dependent elastic deformations, and identify necessary conditions to obtain finite deformations. Finally, we provide a closed form solution for a Green's function corresponding to time periodic actuations, and demonstrate its use in providing analytical and numerical solutions for axially symmetric cases. We show that the deformation field due to time periodic oscillations of the Helmholtz–Smoluchowski slip velocity within a disk results in a deformation field of an exact dipole.

2. Problem formulation

Consider a liquid layer confined between a rigid plate and an elastic plate, in a shallow geometry limit, $h_0 \ll L$, where h_0 is the characteristic gap between the plates and L is the typical lateral in-plane dimension. Figure 1 presents a schematic illustration of the configuration and the orientation of the Cartesian coordinate system we employ, in which the plates are parallel to the x–y plane and z is the normal coordinate to the plates. The total height of the elastic plate relative to the rigid surface is $h = h_0 + \eta$, where η is the deformation of the plate.

We assume that the surface of the rigid plate or the volume between the plates hosts one or more regions where the fluid or wall properties differ from those in the

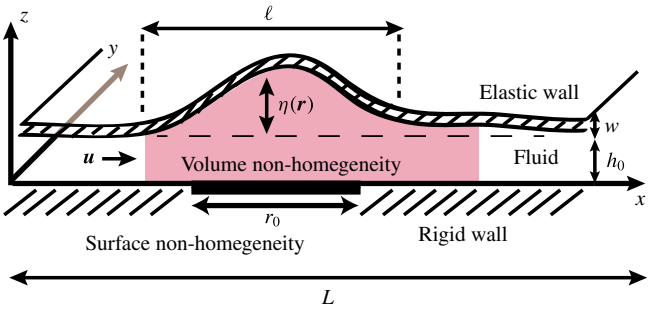

FIGURE 1. (Colour online) Schematic description of a Hele-Shaw configuration, consisting of a thin fluid layer confined between a rigid and an elastic plate of characteristic length L and thickness w, located at an initial distance of h_0 from one another. The fluid is subjected to a spatial non-uniformity in its volume and/or non-uniformity of surface properties on the rigid bottom plane, on a length scale r_0, resulting in a small deformation $\eta \ll h_0$ (drawn not to scale) of the elastic plate, corresponding to the linearized lubrication model. The elastic plate spans a length scale ℓ. The Cartesian coordinate system is chosen such that the plates are in the x–y plane.

surrounding region, and that the typical size of this region is much larger than the distance between the plates, h_0, yet much smaller than the size of the plate,

$$h_0 \ll r_0 \ll L. \tag{2.1}$$

Typical examples of surface quantities that may admit non-uniform behaviour are slip velocity over surfaces with non-uniform zeta potential or slip length over hydrophobic surfaces. Variations in bulk quantities may correspond to viscosity changes due to localized heating, or electric body forces due to application of an external electric field. In this section, we will determine the resulting flow and pressure distribution due to the presence of such non-homogeneities.

Our starting point is the Navier–Stokes equations,

$$\rho\left(\frac{\partial U_i}{\partial t} + U_j\frac{\partial U_i}{\partial x_j}\right) = -\frac{\partial p}{\partial x_i} + \frac{\partial}{\partial x_j}\left[\mu\left(\frac{\partial U_i}{\partial x_j} + \frac{\partial U_j}{\partial x_i}\right)\right] + F_i, \tag{2.2}$$

accompanied by the non-compressibility condition,

$$\frac{\partial U_i}{\partial x_i} = 0, \tag{2.3}$$

where, U_i, F_i, ρ, p and μ are the fluid velocity components, body force components, density, pressure and dynamic viscosity respectively. The indices i, j run over the three Cartesian coordinates x, y, z, and the summation convention over repeated indices is employed. We decompose all three-dimensional vector fields such as fluid velocity, $\boldsymbol{U}$, and body force, $\boldsymbol{F}$, into in-plane components (x, y) and an out-of-plane component (z), using the convention $\boldsymbol{U} = (\boldsymbol{u}, u_z)$ and $\boldsymbol{F} = (\boldsymbol{f}, f_z)$. The dynamics of an elastic plate can be described by the Föppl–von Karman model, which accounts for both bending and tension forces in the plate. Since the ratio of the stretching to bending free energies scales as η^2/w^2, for small deformations ($\eta \ll w$), stretching can

be neglected, leading to the Kirchhoff–Love model (Landau & Lifshitz 1986). This model relates the pressure p and the deformation η according to

$$\rho\frac{\partial^2\eta}{\partial t^2}+D\nabla^4\eta=p,\quad D=\frac{Yw^3}{12(1-\sigma^2)}. \tag{2.4}$$

Here, the bending stiffness coefficient, D, has been expressed in terms of the plate thickness, w, Young's modulus, Y, and Poisson's ratio, σ, and introduces an elastic time scale τ_{EL} according to

$$\tau_{EL}=\ell^2\sqrt{\frac{\rho}{D}}. \tag{2.5}$$

We focus on shallow geometries and small Womersley and reduced Reynolds numbers,

$$\varepsilon=\frac{h_0}{r_0}\ll 1,\quad Wo=\frac{\rho h_0^2}{\mu_0\tau_f}\ll 1,\quad \varepsilon Re=\frac{\rho u^{(0)}h_0^2}{\mu_0 r_0}\ll 1, \tag{2.6a–c}$$

where $Re=\rho u^{(0)}h_0/\mu_0$ is the Reynolds number (Panton 2006) and τ_f is the typical time scale. We assume that the size of the system, L, is much larger than the typical width of the generated deformation, ℓ, which together with the small-deformation assumption combines to

$$\eta\ll w\ll\ell\ll L. \tag{2.7}$$

Normalizing by typical scales,

$$\left.\begin{gathered}\boldsymbol{r}\to\frac{\boldsymbol{r}}{r_0},\quad z\to\frac{z}{h_0},\quad \boldsymbol{u}\to\frac{\boldsymbol{u}}{u^{(0)}},\quad u_z\to\frac{u_z}{u_z^{(0)}},\quad f_z\to\frac{f_z}{\mu_0 u^{(0)}r_0/h_0^3},\\ t\to\frac{t}{\tau_f},\quad \mu\to\frac{\mu}{\mu_0},\quad p\to\frac{1}{\mu_0 u^{(0)}r_0/h_0^2}p,\quad \boldsymbol{f}\to\frac{\boldsymbol{f}}{\mu_0 u^{(0)}/h_0^2},\end{gathered}\right\} \tag{2.8}$$

where $u^{(0)}$, u_z, μ_0 are the typical magnitude of velocity along the plane, the velocity component in the normal direction and the dynamic viscosity respectively. We can rewrite the three-dimensional Navier–Stokes equations, (2.2), in non-dimensional form as

$$\nabla p-\mu\frac{\partial^2\boldsymbol{u}}{\partial z^2}-\boldsymbol{f}=-Wo\frac{\partial\boldsymbol{u}}{\partial t}-\varepsilon Re\left((\boldsymbol{u}\cdot\nabla)\boldsymbol{u}+u_z\frac{\partial\boldsymbol{u}}{\partial z}\right)\varepsilon^2\frac{\partial}{\partial x_\alpha}\left(\mu\frac{\partial}{\partial x_\alpha}\boldsymbol{u}\right), \tag{2.9a}$$

$$\frac{\partial p}{\partial z}-f_z=-\varepsilon^2 Wo\frac{\partial u_z}{\partial t}+\varepsilon^2 Re\left((\boldsymbol{u}\cdot\nabla)u_z+u_z\frac{\partial u_z}{\partial z}\right)+\mu\varepsilon^2\frac{\partial^2 u_z}{\partial z^2}+\varepsilon^4\frac{\partial}{\partial x_\alpha}\left(\mu\frac{\partial}{\partial x_\alpha}u_z\right), \tag{2.9b}$$

where we have assumed that μ does not depend on the vertical coordinate z. Here, the index α runs over the in-plane components x, y, and $\nabla=(\partial/\partial x,\ \partial/\partial y)$ is a two-dimensional gradient. In the leading order of a small reduced Reynolds number, $\varepsilon Re\ll 1$, we can neglect the inertial terms, while in the limit of shallow geometry, $\varepsilon\ll 1$, which is equivalent to $\partial/\partial x_\alpha\ll\partial/\partial z$, we may drop the in-plane derivatives relative to the normal derivative. Together with the assumption that the time scale τ_f is such that the Womersley number is small, we may overlook all inertial terms. Under these assumptions, together with an additional requirement for the normal body

force component to vanish, $f_z = 0$, the three-dimensional nonlinear equations, (2.9), reduce to the following two-dimensional vector and scalar equations:

$$\nabla p - \mu \frac{\partial^2 \boldsymbol{u}}{\partial z^2} - \boldsymbol{f} = 0, \tag{2.10a}$$

$$\frac{\partial p}{\partial z} = 0. \tag{2.10b}$$

The normal component of the velocity is assumed to satisfy the no-penetration condition on the confining walls,

$$u_z|_{z=0} = 0, \quad u_z|_{z=h} = \frac{\partial \eta}{\partial t} + \boldsymbol{u} \cdot \nabla \eta, \tag{2.11a,b}$$

while the tangential components on both planes are subject to either Helmholtz–Smoluchowski slip or Navier slip boundary conditions. Helmholtz–Smoluchowski slip occurs over electrically charged surfaces under an externally applied tangential electric field. The interaction of this field with the excess of net charge in the electric double layer (EDL) results in movement of fluid outside the outer edge of the EDL according to the Helmholtz–Smoluchowski equation (Hunter 2001),

$$\boldsymbol{u}|_{(w)} = -\frac{\epsilon}{\mu} \zeta \boldsymbol{E}, \tag{2.12}$$

where ϵ, ζ, μ and $\boldsymbol{E}$ are the dielectric constant of the liquid, the zeta potential of the confining walls, the dynamic viscosity of the liquid and the tangential imposed electric field respectively. It should be noted that throughout this work we assume a low Dukhin number, such that the ionic species concentrations in the bulk, as well as the associated electric field, are uniform outside the EDL. Otherwise, non-homogeneities of zeta potential and surface conduction introduce non-homogeneity into the resultant electric field in the bulk (Yariv 2004; Khair & Squires 2008). Slip may also emerge over hydrophobic surfaces. Such slip is typically modelled by a Navier boundary condition, which states that the slip velocity near a flat surface is proportional to the local velocity gradient,

$$u|_{(w)} = \beta \left. \frac{\partial u}{\partial n} \right|_{(w)}. \tag{2.13}$$

Here, the parameter β is the so-called slip length, which for simple shear flow corresponds to the fictitious distance inside the solid where the fluid velocity would extrapolate to zero, and n is the normal vector pointing into the fluid. Over the past few decades, experiments and molecular dynamics simulations have indeed confirmed that slip occurs in pressure-driven flows over smooth solvophobic surfaces, with slip lengths of the order of nanometres (Vinogradova 1999; Baudry *et al.* 2001). In this work, we investigate the effect of possible surface non-homogeneities on flow and pressure fields, and allow both types of slip velocities to vary along the surface,

$$\text{Helmholtz–Smoluchowski:} \quad \boldsymbol{u}|_{z=0,h} = \boldsymbol{u}_w^{(0,h)}(\boldsymbol{r}), \tag{2.14a}$$

$$\text{Navier:} \quad \boldsymbol{u}|_{z=0} = \beta(\boldsymbol{r}) \left. \frac{\partial \boldsymbol{u}}{\partial z} \right|_{z=0}, \quad \boldsymbol{u}|_{z=h} = -\beta(\boldsymbol{r}) \left. \frac{\partial \boldsymbol{u}}{\partial z} \right|_{z=h}. \tag{2.14b,c}$$

Integrating (2.10*a*) in the normal direction and utilizing the boundary conditions (2.14*a*) and (2.14*b*,*c*), we obtain

$$\boldsymbol{u}(\boldsymbol{r}, z) = \frac{z(z-h)-\beta h}{2\mu}(\boldsymbol{\nabla} p - \boldsymbol{f}) + \left(1 - \frac{z}{h}\right)\boldsymbol{u}_w^{(0)} + \frac{z}{h}\boldsymbol{u}_w^{(h)}. \tag{2.15}$$

It is important to note that in (2.15) only one boundary condition can be used at a time, i.e. for Helmholtz–Smoluchowski slip velocity β must be set to zero, while for the Navier slip condition $\boldsymbol{u}_w^{(0,h)}$ must be set to zero. Utilizing the kinematic condition $D(z - h(\boldsymbol{r}, t))/Dt = 0$ (where D denotes the substantial derivative), integrating (2.3) along the normal coordinate and utilizing the no-penetration boundary condition yields

$$\frac{\partial h}{\partial t} + \boldsymbol{\nabla} \cdot (h\langle \boldsymbol{u} \rangle) = 0. \tag{2.16}$$

Here, the depth average is defined as $\langle \cdots \rangle = \int_0^h (\cdots)\,\mathrm{d}z / \int_0^h \mathrm{d}z$. Similarly, integrating each of the relations (2.15) and utilizing (2.14), we obtain

$$\langle \boldsymbol{u} \rangle = -\left(\frac{h^2}{12\mu} + \frac{\beta h}{2\mu}\right)(\boldsymbol{\nabla} p - \boldsymbol{f}) + \langle \boldsymbol{u}_w \rangle, \tag{2.17}$$

where $\langle \boldsymbol{u}_w \rangle = (\boldsymbol{u}_w^{(0)} + \boldsymbol{u}_w^{(h)})/2$. Substituting the mean velocity defined in (2.17) into (2.16) and subsequently substituting the pressure from (2.4) yields the nonlinear thin-film approximation,

$$\frac{\partial h}{\partial t} + \boldsymbol{\nabla} \cdot \left[\left(\frac{h^3}{12\mu} + \frac{\beta h^2}{2\mu}\right)(-D\boldsymbol{\nabla}[\nabla^4 h] + \boldsymbol{f}) + h\langle \boldsymbol{u}_w \rangle\right] = 0. \tag{2.18}$$

It should be noted that in neglecting the second-order time derivatives in (2.4) we have inherently assumed that relevant processes occur over time scales much longer than τ_{EL}. Assuming that the deformation is small, i.e. $\eta \ll h_0$, yields the linearized sixth-order diffusion equation,

$$\frac{\partial \eta}{\partial t} - Dh_0 \boldsymbol{\nabla} \cdot (\alpha \boldsymbol{\nabla}[\nabla^4 \eta]) = -h_0 \boldsymbol{\nabla} \cdot (\alpha \boldsymbol{f} + \langle \boldsymbol{u}_w \rangle), \tag{2.19}$$

where $\alpha = h_0^2/(12\mu) + \beta h_0/(2\mu)$. Sixth-order diffusion equations have been employed in the study of various subjects, such as magmal intrusion under a terrestrial crust (Michaut 2011) and interfacial instabilities under elastic membranes (Al-Housseiny *et al.* 2013). From (2.19), the characteristic visco-elastic time scale, τ_{VE}, is given by

$$\tau_{VE} = r_0^6/\alpha D h_0. \tag{2.20}$$

We here examine configurations in which $\tau_{EL} \ll \tau_{VE}$, thus focusing our analysis on visco-elastic effects rather than propagation of elastic waves. Equation (2.20) describes the time scale for the propagation of visco-elastic deformation r_0. However, if the system is actuated on a forced time scale, τ_f, its characteristic length scale of visco-elastic dynamics is determined from (2.20), $r_0 = (\tau_f \alpha D h_0)^{1/6}$. In addition, if the forced time scale is smaller than τ_{VE}, one must ensure that the associated *Wo* number remains sufficiently small.

3. Effect of local non-uniformities in a rigid Hele-Shaw cell

We seek to study the effect of a local variation in the fluid properties on the pressure distribution and flow field due to a combined effect of non-uniform viscosity in the bulk and non-uniform slip velocity on the surface, both described by the following axially symmetric and time-independent functions:

$$\mu(r) = \mu^{(out)} + \Delta\mu \cdot H(R - r), \tag{3.1a}$$

$$\langle \boldsymbol{u}^{(w)}(r) \rangle = \boldsymbol{u}^{(out)} + \Delta\boldsymbol{u}^{(w)} \cdot H(R - r), \tag{3.1b}$$

which are centred at a common point, chosen as the origin of our coordinate system. Here, H stands for a Heaviside step function, R is the distance from the origin at which both quantities experience a transition, and $\Delta\mu = \mu^{(in)} - \mu^{(out)}$ and $\Delta\boldsymbol{u}^{(w)}$ stand respectively for the difference between the values of viscosity and slip velocity in the inner ($r < R$) and outer ($r > R$) regions. Assuming furthermore that only the inner region hosts a Helmholtz–Smoluchowski boundary condition, (2.12), the difference $\Delta\boldsymbol{u}^{(w)}$ between the inner and outer slip velocities is given by

$$\Delta\boldsymbol{u}^{(w)} = -\frac{\epsilon\zeta^{(in)}}{\mu^{(in)}}\boldsymbol{E}. \tag{3.2}$$

While sharp transitions of surface non-homogeneities are expected to introduce deviations from the lubrication approximation, these will be confined to a narrow spatial region of order ε around the transitions (Brotherton & Davis 2004). In our analysis, we overlook these and other deviations due to sharp transition of parameters in the bulk.

For the case of a static elastic plate, the continuity equation (2.16) translates into an incompressibility condition of the two-dimensional depth-averaged flow,

$$\boldsymbol{\nabla} \cdot \langle \boldsymbol{u} \rangle = 0. \tag{3.3}$$

Taking advantage of (3.3), we introduce a stream function ψ defined via $\langle \boldsymbol{u} \rangle = \boldsymbol{\nabla} \times (\psi\hat{z})$ and derive a higher-order differential equation for the pressure by applying the two-dimensional divergence operator to (2.17). Similarly, dividing (2.17) by α and applying the normal component of the curl operator eliminates the pressure. The resultant uncoupled Poisson equations for the pressure and the stream function are given by

$$\boldsymbol{\nabla} \cdot (\alpha\boldsymbol{\nabla}p) = \boldsymbol{\nabla} \cdot [\langle \boldsymbol{u}_w \rangle + \alpha\boldsymbol{f}], \tag{3.4a}$$

$$\boldsymbol{\nabla} \cdot \left(\frac{1}{\alpha}\boldsymbol{\nabla}\psi\right) = \left[\boldsymbol{\nabla} \times \left(\frac{\langle \boldsymbol{u}_w \rangle}{\alpha} + \boldsymbol{f}\right)\right] \cdot \hat{z}. \tag{3.4b}$$

Table 1 in appendix A presents the emergent Poisson equation for several distinct cases.

In the particular case of constant α and vanishing body force, the derived equations (3.4) reduce to two Poisson equations which govern the case of non-uniform slip velocity, derived in Boyko *et al.* (2015). It should be noted that each equation of (3.4) for pressure and stream function is formally equivalent to Gauss' law with a position-dependent dielectric function, where the pressure and stream function play the role of electrostatic potential, and the right-hand sides of (3.4) are interpreted as source terms. Thus, similarly to the case of non-uniform permittivity in electrostatics

(Landau *et al.* 1984), the matching conditions across the common boundary for the pressure and stream function in the case of a piecewise constant distribution of α or $\langle \boldsymbol{u}_w \rangle$ are derived by line integration along an infinitesimal loop across the boundary. Specifically, these matching conditions are constituted by continuity of the potential and its derivative along the tangential direction (denoted by r_t),

$$p^{(in)} = p^{(out)}, \quad \psi^{(in)} = \psi^{(out)}, \tag{3.5a,b}$$

$$\frac{\partial p^{(out)}}{\partial r_t} = \frac{\partial p^{(in)}}{\partial r_t}, \quad \frac{\partial \psi^{(out)}}{\partial r_t} = \frac{\partial \psi^{(in)}}{\partial r_t}, \tag{3.5c,d}$$

and discontinuity of its derivative along the normal direction (denoted by r_n), given by

$$\alpha^{(out)} \frac{\partial p^{(out)}}{\partial r_n} - \alpha^{(in)} \frac{\partial p^{(in)}}{\partial r_n} = -\boldsymbol{\nabla} \cdot [\langle \boldsymbol{u}_w \rangle + \alpha \boldsymbol{f}], \tag{3.6a}$$

$$\frac{1}{\alpha^{(out)}} \frac{\partial \psi^{(out)}}{\partial r_n} - \frac{1}{\alpha^{(in)}} \frac{\partial \psi^{(in)}}{\partial r_n} = -\left[\boldsymbol{\nabla} \times \left(\frac{\langle \boldsymbol{u}_w \rangle}{\alpha} + \boldsymbol{f} \right) \right] \cdot \hat{z}, \tag{3.6b}$$

where the superscripts (*in*) and (*out*) correspond to the two adjacent regions.

The governing equation for the pressure for the case of axially symmetric non-homogeneities in both the viscosity and the Helmholtz–Smoluchowski slip velocity ($\beta = 0$ and $\boldsymbol{f} = 0$) is explicitly written as

$$\frac{1}{r} \frac{\partial}{\partial r} \left(r \frac{\partial p}{\partial r} \right) + \frac{1}{r^2} \frac{\partial^2 p}{\partial \varphi^2} - \frac{1}{\mu} \frac{\mathrm{d}\mu}{\mathrm{d}r} \frac{\partial p}{\partial r} = \gamma \mu \frac{\mathrm{d}}{\mathrm{d}r} \left(\frac{\langle \zeta \rangle}{\mu} \right) \cos(\varphi), \tag{3.7}$$

where φ is the polar angle coordinate and $\gamma = 12E\epsilon/h^2$. The term on the right-hand side suggests a dipole type solution, $p(r, \varphi) = \alpha(r) \cos(\varphi)$, which upon substitution into (3.7), together with (3.1) and (3.2), leads to an ordinary differential equation for $\alpha(r)$, which easily integrates and leads towards the following solution in each of the regions:

$$p^{(in/out)}(r, \varphi) = \left(\frac{a^{(in/out)}}{r} + b^{(in/out)} r \right) \cos(\varphi), \tag{3.8}$$

where $a^{(in/out)}$, $b^{(in/out)}$ are yet to be determined coefficients. Regularity at the origin dictates $a^{(in)} = 0$, while $b^{(out)} = \Delta p / \Delta \ell$ can be identified as a mean pressure gradient applied along the cell, as inferred from boundary conditions at $x \to \pm\infty$. An additional relation between the coefficients can be taken as continuity of pressure or discontinuity of its derivative along the radial direction on the curve $r = R$, constituted respectively by (3.5*a*,*b*) and (3.6*a*), leading to the following expressions for the dipole strength, $a^{(out)}$, and pressure gradient in the inner region, $b^{(in)}$:

$$a^{(out)} = \frac{\Delta p}{\Delta \ell} R^2 \frac{m-1}{m+1} + \frac{12\gamma R^2 \zeta^{(in)}}{m+1}, \tag{3.9a}$$

$$b^{(in)} = 2 \frac{\Delta p}{\Delta \ell} \frac{m}{m+1} + \frac{12\gamma \zeta^{(in)}}{m+1}, \tag{3.9b}$$

where $m = \mu^{(in)}/\mu^{(out)}$. Specific expressions for the pressure and the flow field can be obtained by substituting these coefficients, (3.9*b*), into (2.17) and (3.8).

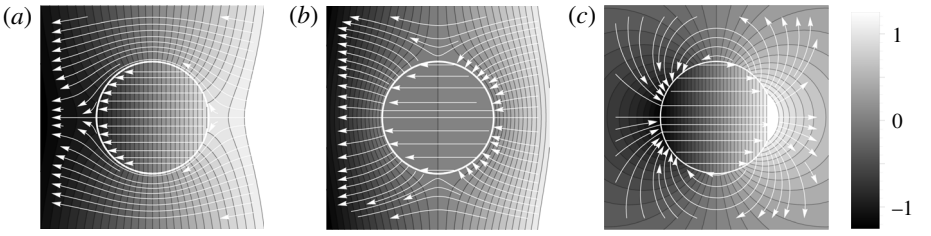

FIGURE 2. Analytical results showing the effect of a disk-shaped non-homogeneity on the resulting pressure distribution (normalized grey-scale colourmap) and flow field (white streamlines). (*a*,*b*) The ratio of internal to external viscosity, m, affects the pressure distribution in the plane. For $m > 1$, (*a*), the density of isobars increases within the disk and decreases outside of it. For $m < 1$, (*b*), the opposite occurs and gradients are smaller within the disk and larger outside of it. In a complementary manner, for $m > 1$, streamlines are repelled from the disk region, whereas $m < 1$ shows a focusing effect, with streamlines attracted to the disk. (*c*) A mismatch in an axial body force, or in EOF slip velocities, between the inner and outer regions of the disk results in a dipole which produces high and low pressures at the edges of the disk.

Figure 2 presents the pressure and flow fields for several cases of spatial non-uniformities. Figures 2(*a*) and 2(*b*) present the cases of increasing ($m > 1$) or decreasing ($m < 1$) the viscosity in the bulk, with vanishing slip velocity throughout. Under a global pressure gradient, the streamlines are repelled from the central region for $m > 1$ and converge for $m < 1$ (as could be anticipated due to the formal analogy between position-dependent $1/\mu$ in Stokes flow and position-dependent dielectric constant in an electrostatic problem). In the limit $m \gg 1$, the radial component of the flow field in the outer region, which is provided in appendix B, vanishes on the surface $r = R$, and the velocity in the inner region tends to zero. Substituting $m = 1$ into (3.9*b*) corresponds to a case of uniform viscosity, and reproduces the electro-osmotic dipole obtained in Boyko *et al.* (2015) with closed streamlines shown in figure 2(*c*). In appendix C, we discuss the use of the Green's function method, which allows us to solve (3.4) for more general cases.

4. Static elastic deformations

Consider static or quasi-static processes characterized by time scales much larger than the characteristic visco-elastic time $r_0^6/\alpha D h_0$, defined in (2.20). The corresponding governing equation for such processes then allows us to neglect partial derivatives with respect to time in (2.19), and for the particular case of non-uniform Helmholtz–Smoluchowski slip velocity it takes the following form:

$$\frac{D h_0^2}{12}\nabla^6\eta = \epsilon\nabla\langle\zeta\rangle\cdot\boldsymbol{E}. \tag{4.1}$$

Since the spatial derivative and the source terms in (2.19) both depend on $1/\mu$, the relation (4.1) between the static deformation and the corresponding zeta potential does not depend on viscosity. For an arbitrary zeta-potential distribution, the deformation field obtained from (4.1) is not necessarily localized and may create deformations with the characteristic length scale of the configuration L. Nevertheless, we may require a localized deformation field and calculate the corresponding zeta potential. For an

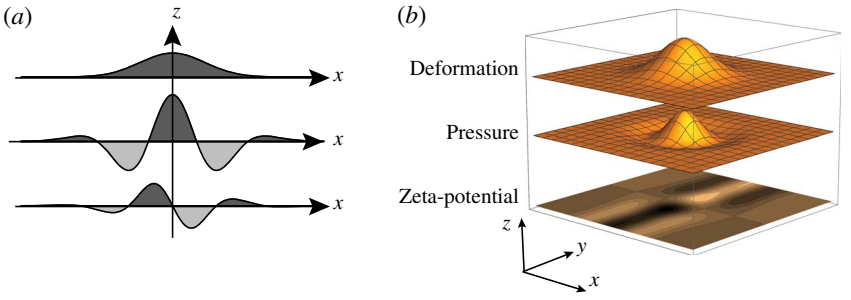

FIGURE 3. (Colour online) Analytical results presenting the zeta potential required for generating a desired Gaussian deformation, and the resulting pressure distribution. Panels (*a*) and (*b*) present the 1D and 2D cases respectively. In both cases, a central region of positive pressure is bracketed by regions of negative pressure to ensure that the deformation remains localized.

electric field E that is homogeneous and oriented along the x direction, we utilize (4.1) to express the zeta potential as a function of the deformation η via

$$\langle \zeta(\boldsymbol{r}) \rangle = \frac{Yw^3h_0^2}{144\epsilon E(1-\sigma^2)} \int (\nabla^6 \eta)\, \mathrm{d}x. \tag{4.2}$$

The integration introduces some function of y, which represents the effects of boundary conditions. In our problem, we assume that the boundaries are sufficiently far from the region of interest, and therefore set this function to zero. Hereafter, we consider the set-up described by figure 1, where the non-homogeneous zeta potential, ζ, resides on the bottom rigid plate. Thus, the mean zeta potential, $\langle \zeta \rangle$, relates to the zeta potential on the bottom plate, ζ, via $\langle \zeta \rangle = \zeta/2$.

Let us determine the pressure and zeta-potential distribution necessary to generate a local deformation of a Gaussian shape,

$$g(\boldsymbol{r}, \boldsymbol{r}_i) = \frac{1}{\pi\sigma^2} \mathrm{e}^{-(\boldsymbol{r}-\boldsymbol{r}_i)^2/\sigma^2}. \tag{4.3}$$

Substituting (4.3) into (2.4) yields an expression for p, while utilizing (4.2) yields the following closed form expression for the necessary zeta-potential distribution:

$$\begin{aligned} \zeta(\boldsymbol{r}) \;=\; & -\frac{8g(\boldsymbol{r})}{\sigma^{10}} \Big[y(12x^4 + 4y^4 - 26y^2\sigma^2 + 33\sigma^4 + 6x^2(2y^2 - 9\sigma^2)) \\ & + \frac{\sqrt{\pi}}{2\sigma} \mathrm{e}^{y^2/\sigma^2} \mathrm{erf}\left[\frac{y}{\sigma}(-8x^6 + 60\sigma^2x^4 - 90\sigma^2x^2 + 15\sigma^6) \right] \Big]. \end{aligned} \tag{4.4}$$

Figures 3(*a*) and 3(*b*) respectively present the one- and two-dimensional zeta-potential distributions necessary to generate the corresponding Gaussian deformation. It should be noted that in both cases the central region with positive pressure distribution is surrounded by regions with negative pressure, which ensure that the total deformation decays to zero on a length scale σ.

To determine the zeta-potential distribution necessary to generate an arbitrary deformation, $f(\boldsymbol{r})$, we take advantage of the linearity of our problem and the finite

Gaussian representation introduced in Gabor (1946), which allows us to approximate any surface as a linear combination of Gaussians centred at different points via $f(\boldsymbol{r}) \simeq \sum_{i=1}^{N} c_i g(\boldsymbol{r}; \boldsymbol{r}_i)$, where the index i identifies a Gaussian centred at a point $\boldsymbol{r}_i$. The coefficients are fixed by demanding that the sum of the Gaussian terms is equal to the values of the function $f(\boldsymbol{r})$ at some N auxiliary points, leading to the following system of N algebraic equations for N coefficients c_i:

$$f(\boldsymbol{r}_j) = \sum_{i=1}^{N} c_i g(\boldsymbol{r}_j; \boldsymbol{r}_i); \quad i, j = 1, 2, \ldots, N, \tag{4.5}$$

where for convenience we set these auxiliary points as the central points of each Gaussian. The approximation in a given domain becomes more accurate as we increase the number of Gaussian terms in the sum and decrease the distances between their central points. The corresponding zeta potential, $\langle \zeta(\boldsymbol{r}) \rangle$, necessary to generate a desired deformation is given by

$$\langle \zeta(\boldsymbol{r}) \rangle \simeq \sum_{i=1}^{N} c_i \langle \zeta(\boldsymbol{r}; \boldsymbol{r}_i) \rangle, \tag{4.6}$$

where each of the $\langle \zeta(\boldsymbol{r}; \boldsymbol{r}_i) \rangle$ terms in the sum above corresponds to the zeta potential needed to maintain a single Gaussian deformation, given by (4.4).

For illustration, consider an example for the one- and the two-dimensional cases, where we determine the zeta potential necessary to create desired deformations which have the shape of a human face and the African continent respectively. Figure 4(*a*) presents the shape of a human face created by a sum of 45 Gaussians, while figure 4(*b*) presents the set of Gaussians multiplied by the corresponding coefficients c_i. Figure 4(*c*) presents the resultant zeta-potential distribution obtained by summing the contribution needed to create each one of the Gaussians, by utilizing (4.6). Following the same steps, it is possible to obtain the two-dimensional zeta-potential distribution necessary to create arbitrary deformation profiles in 2D. Figure 4(*d*) presents the result of summing 400 Gaussians, while figure 4(*e*) presents the corresponding zeta potential obtained by inserting the zeta potential needed to support each one of Gaussians, (4.4), into the sum (4.6).

5. Time-dependent elastic deformations

Consider the general elastic deformations equation, (2.19), where the only spatial non-homogeneity is in the Helmholtz–Smoluchowski slip velocity (i.e. $\boldsymbol{f} = 0$ and $\beta = 0$), and the source term is then the component of the zeta-potential gradient along the electric field. For convenience, we scale to dimensionless variables via $\boldsymbol{r} \to r_0 \boldsymbol{r}$, $\eta \to \eta_0 \eta$, $t \to \tau_{VE} t$, $E \to E_0 E$ and $\zeta \to \zeta_0 \zeta$. The equation then takes the form of a sixth-order diffusion equation,

$$\frac{\partial \eta}{\partial t} - \nabla^6 \eta = \kappa \nabla \langle \zeta \rangle \cdot \boldsymbol{E}, \tag{5.1}$$

where $\kappa = \epsilon_0 u_0 \tau_{VE} / \eta_0$, $\epsilon_0 = h_0 / r_0$, $u_0 = \epsilon \zeta_0 E_0 / \mu$ is the typical slip velocity, and τ_{VE} is defined by (2.20). Similarly to (4.2), an explicit expression for the zeta potential required to generate pre-assigned spatio-temporal elastic deformations, $\eta(\boldsymbol{r}, t)$, can be

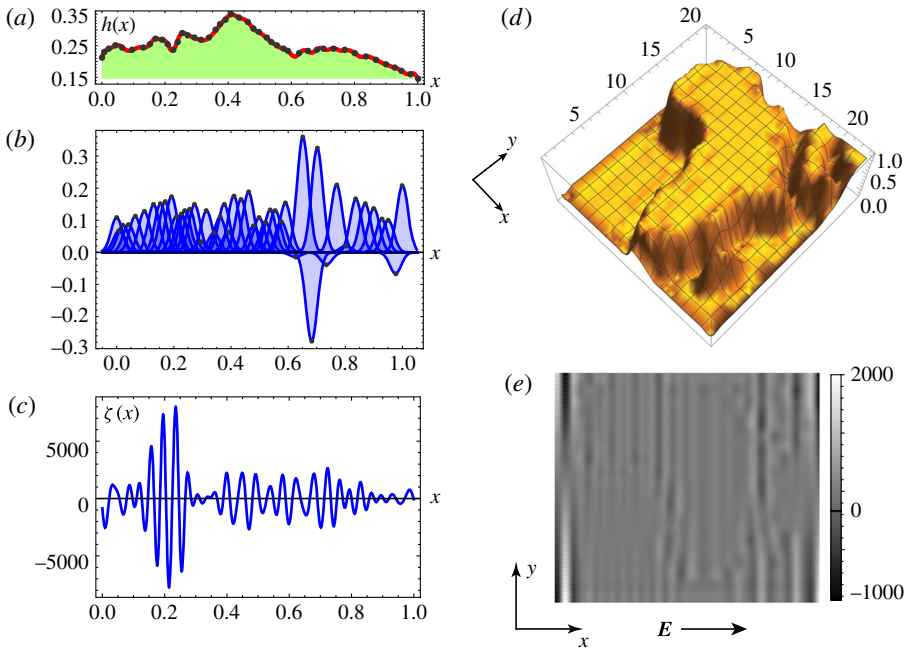

FIGURE 4. (Colour online) Analytical results demonstrating the calculation of zeta-potential distributions required in order to create complex deformations. (*a*) A smooth curve of a human face profile, which is generated by superposition of 45 Gaussians, presented in (*b*). (*c*) The total zeta-potential distribution required to generate this deformation. (*d*) The sum of 400 Gaussians (20×20 array) is used to describe a deformation corresponding to the topography of the African continent. (*e*) The zeta-potential distribution (colourmap) in the x–y plane required to achieve this deformation.

obtained by expressing the corresponding zeta potential, $\zeta(\boldsymbol{r}, t)$, from the right-hand side of (5.1) through the following integral:

$$\langle \zeta(\boldsymbol{r}, t) \rangle = \frac{1}{\kappa E} \int \left(\frac{\partial \eta(\boldsymbol{r}, t)}{\partial t} - \nabla^6 \eta(\boldsymbol{r}, t) \right) \mathrm{d}x, \tag{5.2}$$

where we have assumed that the external electric field is uniform and is applied along the x-axis. The resultant expression for $\zeta(\boldsymbol{r}, t)$ in such cases is a sum of two terms. The first term expresses the zeta potential required to sustain the rate of deformation and the second term represents the zeta potential of the static problem (i.e. $\partial\eta/\partial t = 0$), given by (4.2).

5.1. *Asymptotically static transient deformations*

A particularly useful family of solutions are asymptotically static deformations, where $\partial\eta/\partial t \to 0$ as $t \to \infty$. Such deformations correspond, for example, to transitions from a non-deformed initial condition ($\eta = 0$) to one of the static solutions described in the previous section.

For illustration, let us determine the necessary zeta potential to actuate an asymptotically static deformation, $\eta_0(\boldsymbol{r}, t)$, that is set in a separable form of the type $\eta_0(\boldsymbol{r}, t) = g(\boldsymbol{r})T(t)$, where $g(\boldsymbol{r})$ is a Gaussian function and $T(t) = \tanh(t)$ (see

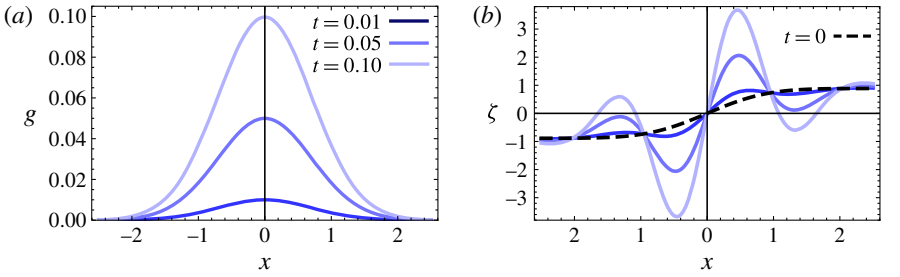

FIGURE 5. (Colour online) Analytical result showing the zeta-potential distribution required to smoothly transition from a non-deformed membrane to a Gaussian deformation. (*a*) We define the desired deformation as $\eta_0(\boldsymbol{r}, t) = g(\boldsymbol{r})T(t)$, where $g(\boldsymbol{r})$ is a Gaussian and $T(t)$ is a smooth function which asymptotes to unity for $t \to \infty$ (here, $T(t) = \tanh(t)$). (*b*) The required zeta potential at several early time points. For early times, the term associated with the rate of transition in (5.2) dominates, whereas at $t \to \infty$ the zeta potential asymptotes to the static solution, as given by (4.2).

figure 5*a*). The corresponding expression for the zeta potential is the sum of the solution to the static problem, (4.2), multiplied by $\tanh(t)$, and of the term due to explicit dependence in time, $(\sqrt{\pi}\sigma/(2\cosh^2(t)))\mathrm{erf}(x/\sigma)$. As shown in figure 5(*b*), the latter indeed tends to zero as time increases, and at late times the zeta potential tends to the solution of the static problem.

5.2. *Transient deformations due to a spatially localized zeta-potential distribution*

We now examine the resultant elastic deformations due to zeta-potential distributions that do not generate asymptotically static deformations. The governing equation for deformations in the case where the source term on the right-hand side of (5.1) represents localized actuation is of the form

$$\frac{\partial \eta}{\partial t} - \nabla^6 \eta = f(t)\delta(\boldsymbol{r}), \tag{5.3}$$

where $\delta(\boldsymbol{r})$ is the Dirac delta function and $f(t)$ is an arbitrary function of the time parameter which vanishes for $t < 0$. Here and in the following, without loss of generality, we set $\kappa = 1$. First, we investigate the resultant deformation $\eta_H(\boldsymbol{r}, t)$ for the case of sudden actuation $f(t) = H(t)$, where $H(t)$ is the Heaviside function. It should be noted that since in this case the source term on the right-hand side of (5.3) does not contain any time scale or length scale, we expect this case to exhibit a self-similar behaviour. Indeed, under scaling of time and space variables via $t \to \alpha t$ and $\boldsymbol{r} \to \beta \boldsymbol{r}$, where α and β are constants, the transformation law of the Heaviside and Dirac delta functions is given by $H(\alpha t) = H(t)$ and $\delta(\beta \boldsymbol{r}) = (1/\beta^2)\delta(\boldsymbol{r})$. Assuming furthermore that η_H has no poles at $r = 0$ or at $r = \infty$, and demanding that (5.3) with $f(t) = H(t)$ is invariant under a similarity transformation, leads to

$$\eta_H(\boldsymbol{r}, t) = t^{2/3} W(\xi), \quad \xi = \frac{(r/6)^6}{t}, \tag{5.4}$$

where W is a function of the dimensionless variable ξ, and the factor of six is introduced for convenience. In appendix D, we derive a closed form expression for η_H and discuss the Green's function solutions. (That is, solutions to (5.3) where $f(t) = \delta(t)$. Such solutions have also been studied in Tulchinsky & Gat (2015).) For a fixed value of the similarity variable ξ, the function η_H is a diverging function for increasingly large values of the variable t.

5.3. *Time-dependent deformation due to an oscillating actuation*

We now consider time-dependent deformations driven by a harmonic source with a typical time period $\tau_f = 1/\omega$. In particular, we consider the dynamics after a sufficiently long time τ_0, such that all transient solutions have decayed, i.e. $\tau_0 > L^2/Dh_0\alpha$, where L is a characteristic size of the system. Importantly, the effect of an oscillating electric field with an angular frequency $1/\tau_f$ is inherently limited by the momentum diffusion time scale $\rho h_0^2/\mu$. Hence, quasi-stationarity of the flow in the alternating field regime translates into a condition $\omega < \mu/\rho h_0^2$, which poses an upper bound on possible angular frequency (Minor *et al.* 1997).

The governing equation (5.1) for the one-dimensional and time-dependent actuation is described by

$$\frac{\partial \eta}{\partial t} - \frac{\partial^6 \eta}{\partial x^6} = \mathrm{e}^{\mathrm{i}\omega t}\delta(x), \tag{5.5}$$

which corresponds to a case where two adjacent half-spaces, with a common boundary along the $x = 0$ line, host different values of the zeta potential. The time dependence can stem from time-varying zeta potential or applied electric field, or both. Assuming that the solution admits harmonic time behaviour $\mathrm{e}^{\mathrm{i}\omega t}$, we employ the Fourier transform method and derive the following representation for the deformation:

$$\eta(x, t) = \frac{\mathrm{e}^{\mathrm{i}\omega t}}{2\pi} \int_{-\infty}^{\infty} \frac{\cos(kx)}{k^6 + \mathrm{i}\omega}\, \mathrm{d}k. \tag{5.6}$$

Utilizing the residue theorem for the choice $\omega > 0$ and $x > 0$, we obtain the following closed form expression for the real part of $\eta(x, t)$:

$$\begin{aligned} \eta(x, t) \;=\; & \frac{1}{\omega^{5/6}} \mathrm{e}^{-p_- \omega^{1/6} x} \left[\sin\left(\omega t - p_+ \omega^{1/6} x + \frac{\pi}{6}\right) \right. \\ & + \mathrm{e}^{-\sqrt{3} p_- \omega^{1/6} x} \sin\left(\omega t - (p_+ - p_-)\omega^{1/6} x + \frac{\pi}{6}\right) \\ & \left. + \mathrm{e}^{-(p_+ - p_-)\omega^{1/6} x} \cos(\omega t - p_- \omega^{1/6} x) \right], \end{aligned} \tag{5.7}$$

where $p_\pm$ are positive constants given by

$$p_\pm = \frac{\sqrt{3} \pm 1}{2\sqrt{2}}. \tag{5.8}$$

The solution (5.7) is a sum of three exponentially damped sinusoidal waves, travelling with different group velocities which scale as $\omega^{5/6}$. Figure 6(*a*) presents the solution, (5.7), at different times. Asymptotic behaviour at large values of x singles out the first term in (5.7), characterized by having the smallest exponential damping factor. At the origin, the motion is purely sinusoidal with angular velocity ω and normalized amplitude $\sqrt{7}$. It should be noted that the three different terms in the periodic solution (5.7) stem from the locations of three simple poles in the upper complex plane. This can be compared with the solution for the simpler case of a standard diffusion equation driven by a harmonic source (i.e. (5.5) with second-order spatial derivative), which consists of a single pole in the upper complex plane and therefore a single exponentially damped term. In the limit of large ω, which in the dimensionless units we use in this section corresponds to $\tau_f \ll \tau_{VE}$, at the origin the characteristic

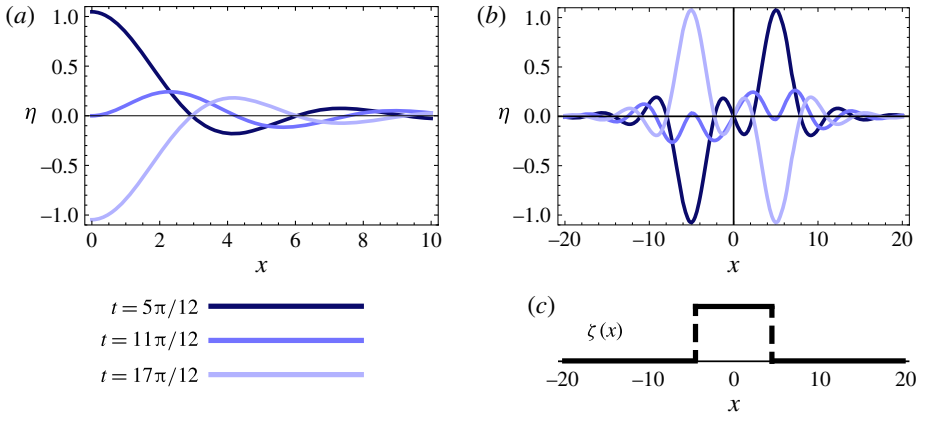

FIGURE 6. (Colour online) (*a*) Analytical results showing exponentially damped diffusion waves due to a localized oscillating source at the origin at times $t = 5\pi/12$, $11\pi/12$, $17\pi/12$. (*b*) A stripe-shaped distribution of the zeta potential, in which the non-zero value of the zeta potential is within a finite interval (as shown in (*c*)), gives rise to two opposite-sign sources in (5.5) located at the edges of the strip. The solution is an odd function and the central point $x = 0$ remains stationary throughout the motion.

amplitude of the solution approaches zero as $\omega^{-5/6}$. Clearly, there is also a lower limit on the value of ω which is determined by the physical dimensions of the system.

As an example, consider the deformation due to time periodic actuation of the zeta potential within a finite width stripe of width $2w$ (figure 6*c*), created by a source composed of two opposite-sign Dirac delta functions, located at the two edges of the strip. Employing linearity of the governing equation, we can then superpose the single-source solution at different positions and write the resulting solution as $\eta(x + w, t) - \eta(x - w, t)$, where η represents a solution of type (5.7) due to each one of the sources. The solution at several time points is presented in figure 6(*b*). It should be noted that due to asymmetry, this solution vanishes at the origin at all times, and therefore in each of the regions $x \leqslant 0$ and $x \geqslant 0$ the solution describes deformation due to a zeta-potential distribution within a stripe of width w in the presence of a fixed boundary condition (e.g. rigid wall) at $x = 0$. Applying a standard image method, one can construct a solution due to an oscillating source in the presence of more complex boundaries (e.g. two walls).

A similar approach can be taken to extend the previous results to the two-dimensional case of a spatially localized and time periodic actuation. The governing equation (5.1) takes the following form:

$$\frac{\partial \eta}{\partial t} - \nabla^6 \eta = \mathrm{e}^{\mathrm{i}\omega t}\delta(\boldsymbol{r}). \tag{5.9}$$

Its solution can be found by standard methods of Fourier transform and complex integration, and is explicitly given by

$$\eta(r, t) = \mathrm{e}^{\mathrm{i}\omega t} G^{4,0}_{0,6}\left(0, \frac{1}{3}, \frac{2}{3}, \frac{2}{3}, 0, \frac{1}{3}\middle| \mathrm{i}\omega\left(\frac{r}{6}\right)^6\right), \tag{5.10}$$

where $G^{m,n}_{p,q}$ is the so-called Meijer G-function (see Olver 2010, and references within).

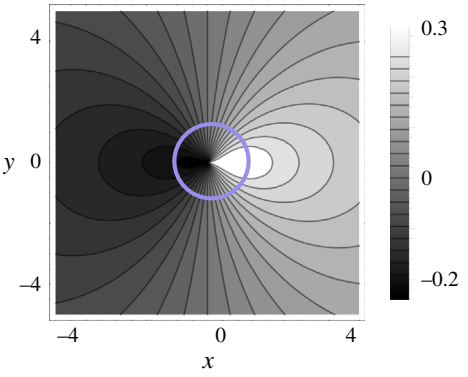

FIGURE 7. (Colour online) Numerical result showing the deformation of an elastic plate resulting from a disk-shaped zeta-potential distribution of radius unity (within the blue circle) subjected to an oscillating electric field along the x-axis. The deformation assumes a $\cos(\varphi)$ angular dependence of the dipole, as can be anticipated from the $\cos(\varphi)$ term on the right-hand side of (5.11).

It should be noted that, in contrast to the one-dimensional case, the source term on the right-hand side of (5.9) does not correspond to a physical zeta-potential distribution. The latter follows from the fact that any two adjacent regions that host different values of zeta potential always introduce a zeta-potential gradient along a common boundary curve, and never along a single point. Nevertheless, we can still utilize the solution (5.10) and the superposition principle, to consider more complex study cases in 2D, such as that of a deformation due to an oscillating value of the Helmholtz–Smoluchowski slip velocity within a disk of radius r_0 (due to oscillation of either the zeta potential or the external electrical field), subject to

$$\frac{\partial \eta}{\partial t} - \nabla^6 \eta = \mathrm{e}^{\mathrm{i}\omega t}\delta(r - r_0)\cos(\varphi). \tag{5.11}$$

In appendix E, we show that the solution to (5.11) admits an angular dependence of a dipole. In particular, we show that the line integration of all $\cos(\varphi)$ weighted sources along a circle (5.11) takes the form $\eta(\boldsymbol{r}, t) = \mathrm{e}^{\mathrm{i}\omega t}R(r)\cos(\varphi)$, and provide a closed form expression for $R(r)$ in terms of Gauss hypergeometric functions. As shown in figure 7, a numerical solution can be obtained by convolving the Green's function solution (5.10) with $\cos(\varphi)$ along a circle.

6. Concluding remarks

In this work, we studied non-uniform lubrication flows in the gap between a rigid plate and a parallel elastic plate as a mechanism to create time-varying deformation fields of the elastic plate. The approach we presented can be relevant to various applications such as adaptable optics, soft actuators and lab-on-a-chip devices. It is instructive to estimate the resultant deformation for realistic parameters. For actuation due to EOF-driven Helmholtz–Smoluchowski slip velocity, and using typical values of the zeta potential of $\zeta = 50$ [mV] (i.e. nearly twice the thermal voltage $V_T \sim 25.6$ [mV]), the plate Young modulus $Y = 1$ [mPa] corresponding to polydimethylsiloxane (PDMS) (Cheng *et al.* 2010), the magnitude of the applied

electric field $E = 10^4$ [V m^{-1}], the gap between the plates $h_0 = 50$ [μm], the plate thickness $w = 10$ [μm] and the dielectric constant $\epsilon = 80\varepsilon_0$ (where ε_0 is the dielectric permittivity of the vacuum), we obtain a deformation η of the order of 40 [μm] distributed over a region of width 300 [μm]. Naively, from the linearity of (5.1), one could expect that an order of magnitude increase of the zeta potential would lead to a similar increase in the deformation. However, as can be directly obtained by the Boltzmann distribution for the monovalent ion concentration in the EDL, $c_{EDL}/c_0 = \mathrm{e}^{\zeta/V_T}$, together with the fact that the ions have a finite size, there exists an upper bound for ζ above which it is not possible to pack additional charges into the EDL. For example, a bulk solution concentration of $c_0 = 1$ [mM] would reach the critical packing limit on the surface at approximately $\zeta = 350$ [mV], and is expected to introduce corrections even at lower values of the zeta potential (Bazant *et al.* 2009). Indeed, Van Der Wouden *et al.* (2005) reported saturation in EOF velocity for sufficiently high zeta potentials.

In §§ 4 and 5, we examined static and asymptotically static deformations. Such deformations are achieved by requiring a steady deformation field within a defined finite region and then calculating the corresponding zeta-potential distribution. In such configurations, the deformations vanish outside of the deformed region, and thus boundary conditions can be applied near the deformed region without affecting the solution. Thus, the requirement $\ell \ll L$ (stating that the configuration characteristic length L is much greater than the characteristic length ℓ of the deformed region) is unnecessary for static and asymptotically static spatially localized solutions.

Our analysis of localized steady zeta-potential actuation yielded a solution that grows indefinitely with time, which indicates that these solutions are no longer valid after a certain time, as they fail to satisfy the underlying assumptions of our model. In practice, there are several stabilizing mechanisms such as physical walls and the liquid's own weight, which impose restoring forces on the elastic plate and are expected to prevent the diverging behaviour, though investigation of such models lies beyond the scope of this study. Within the small-deformation regime used in this work, the static solutions are valid provided that $\eta_L/\eta_\ell \sim p_L L^4 p_\ell \ell^4 \ll 1$, where the subscript ℓ indicates the deformation and pressure associated with the localized solution, whereas L indicates quantities associated with the perturbation field over the entire configuration.

In this work, we focused on deformations that were small compared with the gap between the plates, which allowed us to consider one-way coupling between the fluid pressure and the elastic deformation of the plate. From our order of magnitude analysis, it appears feasible to obtain pressures that would result in deformations of a few tens of microns. In principle, it is possible to achieve larger deformations by utilizing a thinner elastic plate (at least in the Kirchhoff–Love model the deformation depends on the thickness in a power of three) and/or utilizing more compliant materials which may become more available with the advance of materials science (e.g. materials with Young modulus $Y \sim 1$ [kPa], reported in Moraes *et al.* (2015)). The modelling of large deformations is an interesting extension of this work where one must consider changes in the flow field and the electric field due to deformations, as well as account for additional elastic forces such as the tension in the plate (which could be captured by the Föppl–von Karman model), and also body forces such as gravity, which are expected to have an additional stabilizing effect on the dynamics of the plate.

Quantity	Governing equation	Non-uniform and vanishing quantities
Helmholtz–Smoluchowski slip velocity	$\nabla^2 p - \dfrac{12\mu}{h^2}\boldsymbol{\nabla}\cdot\langle\boldsymbol{u}_w\rangle = 0$	$\langle\boldsymbol{u}_w\rangle = \langle\boldsymbol{u}_w(\boldsymbol{r})\rangle,\ \boldsymbol{f}=0,\ \beta=0$
Viscosity	$\boldsymbol{\nabla}\cdot\left(\dfrac{1}{\mu}\boldsymbol{\nabla}p\right)=0$	$\mu=\mu(\boldsymbol{r}),\ \boldsymbol{f}=0,\ \beta=0,\ \langle\boldsymbol{u}_w\rangle=0$
Navier slip velocity	$\boldsymbol{\nabla}\cdot\left(\left(1+\dfrac{12\beta}{h}\right)\boldsymbol{\nabla}p\right)=0$	$\beta=\beta(\boldsymbol{r}),\ \boldsymbol{f}=0,\ \langle\boldsymbol{u}_w\rangle=0$
Body force	$\nabla^2 p+\boldsymbol{\nabla}\cdot\boldsymbol{f}=0$	$\boldsymbol{f}=\boldsymbol{f}(\boldsymbol{r}),\ \langle\boldsymbol{u}_w\rangle=0,\ \beta=0$

TABLE 1. Simplified governing equations for the pressure, obtained from (3.4*a*) for specific choices of space-dependent fluid properties.

Acknowledgements

This project has received funding from the European Research Council (ERC) under the European Union's Horizon 2020 Research and Innovation Programme, grant agreement no. 678734 (MetamorphChip). We gratefully acknowledge support by the Israel Science Foundation (grant no. 818/13). S.R. was supported in part by a Technion fellowship from the Lady Davis Foundation.

Appendix A. Governing equation for several specific cases of non-homogeneous quantities

In § 2, we derived a pair of uncoupled Poisson equations, (3.4), for the pressure and the stream function of the depth-averaged flow. Table 1 summarizes a few cases where physical quantities experience non-uniform behaviour on the surface or in the bulk, along with the corresponding governing equations for the pressure.

Appendix B. Flow field for the case of non-uniform viscosity

In § 3, we derived an expression for the pressure distribution due to a disk-shaped region where both the viscosity and the Helmholtz–Smoluchowski slip velocity take values that are different from the values in the surrounding region (3.8), (3.9*b*). Inserting this expression into the depth-averaged momentum equation, (2.17), yields the corresponding depth-averaged velocity $\langle\boldsymbol{u}\rangle$. For the particular case in which only the viscosity is non-homogeneous (i.e. the slip velocity remains uniform throughout the domain), the corresponding velocity fields in the outer and inner regions are given by

$$\langle\boldsymbol{u}^{(out)}\rangle = (u_r^{(out)}, u_\theta^{(out)}) = \frac{h^2}{12\mu^{(out)}}\frac{\Delta p}{\Delta\ell}\left(\left[\frac{R^2}{r^2}\frac{m-1}{m+1}-1\right]\cos(\theta),\ \left[\frac{R^2}{r^2}\frac{m-1}{m+1}+1\right]\sin(\theta)\right), \tag{B 1}$$

$$\langle\boldsymbol{u}^{(in)}\rangle = (u_x^{(in)}, u_y^{(in)}) = -\frac{h^2}{6\mu^{(in)}}\frac{\Delta p}{\Delta\ell}\left(\frac{m}{m+1}, 0\right). \tag{B 2}$$

Appendix C. Calculation of the pressure field by line integration of the Green's function

In § 3, we determined the pressure due to a disk-shaped non-homogeneity of viscosity and Helmholtz–Smoluchowski slip velocity by solving the governing equations (3.4) in each of the regions and then utilizing the matching conditions (3.5). In a more general configuration, however, it is not always possible to perform direct integration of (3.4), and alternative methods are necessary. The Green's function method, which relies on the linearity of the governing equations, is particularly well suited for our problem. As was noted below (5.10), physically meaningful sources in piecewise constant distributions are always distributed along curves, and the source to the Green's function itself (prior to the convolution integral) does not have a physical meaning.

Here, we demonstrate the use of the Green's function method for re-deriving the dipole solution due to a disk-shaped non-homogeneity and determine the resultant pressure due to a square-shaped distribution of non-uniform Helmholtz–Smoluchowski slip velocity. To this end, we utilize the following expression for the Green's function for the two-dimensional Laplacian (Olver 2010):

$$G(\boldsymbol{r},\boldsymbol{r}')=\frac{1}{2\pi}\ln|\boldsymbol{r}-\boldsymbol{r}'|. \tag{C 1}$$

Consequently, the corresponding expression for the pressure $p(\boldsymbol{r})$, due to the distribution of point sources along the curve γ with a source of strength $F(\boldsymbol{r})$, is given by the following line integral along Γ:

$$p(\boldsymbol{r})=\gamma\int_{\Gamma}G(\boldsymbol{r}-\boldsymbol{r}')F(\boldsymbol{r}')\,\mathrm{d}\boldsymbol{r}', \tag{C 2}$$

where γ is a constant (see the text above (3.8)).

C.1. *Disk-shaped non-homogeneity*

Substituting the Green's function solution, (C 1), into (C 2) and integrating along a circle of radius R, with $F(\boldsymbol{r}')$ being proportional to $\cos(\varphi')$, leads to

$$p=-\frac{E\zeta_0 R}{4\pi}\int_0^{2\pi}\mathrm{d}\varphi'\ln(R^2+r^2-2Rr\cos(\varphi-\varphi'))\cos(\varphi'). \tag{C 3}$$

Transforming the summation angle variable via $\tilde{\varphi}=\varphi-\varphi'$, we obtain

$$p=-\frac{E\zeta_0 R}{4\pi}\int_0^{2\pi}\mathrm{d}\tilde{\theta}\ln(R^2+r^2-2Rr\cos(\tilde{\varphi}))(\cos(\tilde{\varphi})\cos(\varphi)-\sin(\tilde{\varphi})\sin(\varphi)), \tag{C 4}$$

yielding

$$p=\begin{cases}\dfrac{E\zeta_0 R^2}{r}\cos(\varphi), & \text{if } R>r,\\ E\zeta_0 r\cos(\varphi), & \text{if } R<r,\end{cases} \tag{C 5}$$

which coincides with the solution, (3.9*b*), for the case $m=1$.

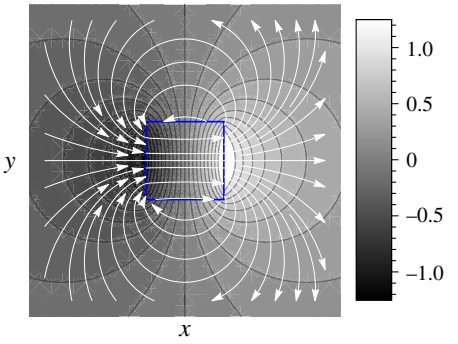

FIGURE 8. (Colour online) Analytical result showing the pressure distribution (colourmap) given by (C 6) and the flow field (white) due to a constant zeta potential within a square region (square boundary shown in blue) under a uniform electric field along the x direction.

C.2. *Square-shaped non-homogeneity*

Consider a non-axially-symmetric case where the Helmholtz–Smoluchowski slip velocity is zero everywhere except inside a square-shaped region. Assuming that the electric field is along the x direction, two sides of the square are perpendicular to the x direction, and following (C 2) we derive the following expression for the resultant pressure:

$$p(\boldsymbol{r}) = f\left(\boldsymbol{r}; -\frac{L}{2}, \frac{L}{2}\right) - f\left(\boldsymbol{r}; -\frac{L}{2}, -\frac{L}{2}\right) - \left(f\left(\boldsymbol{r}; \frac{L}{2}, \frac{L}{2}\right) - f\left(\boldsymbol{r}; \frac{L}{2}, -\frac{L}{2}\right)\right), \quad \text{(C 6)}$$

where

$$f(\boldsymbol{r}; \boldsymbol{r}_0) = \frac{\gamma}{2\pi}\left((x-x_0)\tan^{-1}\left(\frac{x-x_0}{y-y_0}\right) + (y-y_0)\left(1 - \log\left(\sqrt{(x-x_0)^2 + (y-y_0)^2}\right)\right)\right). \quad \text{(C 7)}$$

Figure 8 presents the analytical solution for the pressure distribution (colourmap) and the corresponding flow-field lines (white). Following similar steps, the solution can be easily extended to determine the pressure and flow field due to constant values of other non-homogeneities in a polygon-shaped region.

Appendix D. Derivation of the time-dependent Green's function and the actuation due to a suddenly applied source

In § 5, we performed scaling analysis of (5.3) for the case of Heaviside actuation (i.e. $f(t) = H(t)$), and concluded that the corresponding solution, η_H, diverges in time as $t^{2/3}$. In this appendix, we derive the specific closed form solution of the function η_H (in 1D and 2D) and also numerically analyse the case of a spatially localized actuation that decays in time.

Important for our derivation of η_H is the observation that this function can be expressed as an indefinite time integral of the Green's function, η_D, that solves the following equation for $t > 0$:

$$\frac{\partial \eta_D}{\partial t} - \nabla^6 \eta_D = \delta(t)\delta(\boldsymbol{r}). \quad \text{(D 1)}$$

Therefore, instead of directly integrating (5.3) (for $f(t) = H(t)$), we can integrate η_D, which has been derived for the 2D case in Tulchinsky & Gat (2015). For completeness, we also provide closed form expressions for the Green's function in the 1D case.

D.1. *Transient deformation due to Heaviside actuation*

It is useful to consider the properties of (D 1) under the scaling transformation $t \to \alpha t$, $\boldsymbol{r} \to \beta \boldsymbol{r}$. Similarly to our discussion below (5.4), scaling, utilizing $\delta(\alpha t)\delta(\beta \boldsymbol{r}) \to (1/\alpha\beta^2)\delta(t)\delta(\boldsymbol{r})$ and demanding that (D 1) is invariant under the scaling transformation yields

$$\eta_D(\boldsymbol{r}, t) = \frac{1}{t^{1/3}} U(\xi), \quad \xi = \frac{(r/6)^6}{t}. \tag{D 2}$$

Since η_D is analytic for $t > 0$, the specific form (D 2) allows us to expand it in the following series:

$$\eta_D(\boldsymbol{r}, t) = \frac{1}{t^{1/3}} \sum_{m=0}^{\infty} c_m \left(\frac{r^2}{t^{1/3}} \right)^m. \tag{D 3}$$

To determine the closed form expression for η_D, we note that the Laplace transforms of (D 1) and the homogeneous equation $\partial \eta_d / \partial t - \nabla^6 \eta_d = 0$, subject to the initial condition $\eta_d|_{t=0} = \delta(\boldsymbol{r})$, are identical, and their solutions are related via $\eta_D(\boldsymbol{r}, t) \equiv H(t)\eta_d(\boldsymbol{r}, t)$. The solution to the homogeneous problem, η_d, is easily found by summing complex separable solutions $\mathrm{e}^{-k^6 t}\mathrm{e}^{\mathrm{i}\boldsymbol{k}\cdot\boldsymbol{r}}$, for different values of the wavevector $\boldsymbol{k}$ (identically to the 2D heat equation). Given the fact that in our problem there are no boundary conditions, we meet no restrictions on the choice of wavevectors, and therefore lead towards the following integral expressions for the Green's function in 1D and 2D (for $t > 0$):

$$\eta_D(x, t) = \frac{1}{2\pi} \int_{-\infty}^{\infty} \mathrm{e}^{-k^6 t}\mathrm{e}^{\mathrm{i}kx}\, \mathrm{d}k \ \text{ in } \ 1\mathrm{D}, \tag{D 4}$$

$$\eta_D(\boldsymbol{r}, t) = \frac{1}{2\pi} \int_{-\infty}^{\infty} \left[\int_0^{2\pi} \mathrm{e}^{-k^6 t}\mathrm{e}^{\mathrm{i}kr\cos(\varphi)}\, \mathrm{d}\varphi \right] k\, \mathrm{d}k \ \text{ in } \ 2\mathrm{D}. \tag{D 5}$$

The integral expression for the Green's function in 2D, (D 5), admits the following representation in terms of three hypergeometric functions:

$$\begin{aligned} \eta_D(\boldsymbol{r}, t) \ = \ & \frac{\Gamma\left(\frac{1}{3}\right)}{6t^{1/3}}\, {}_0F_4\left(\frac{1}{6}, \frac{1}{2}, \frac{2}{3}, \frac{5}{6}; -\xi\right) - \frac{r^2\Gamma\left(\frac{2}{3}\right)}{12t^{2/3}}\, {}_0F_4\left(\frac{1}{2}, \frac{5}{6}, \frac{7}{6}, \frac{4}{3}; -\xi\right) \\ & - \frac{r^4}{144t}\, {}_1F_5\left(1; \frac{5}{6}, \frac{7}{6}, \frac{4}{3}, \frac{3}{2}, \frac{5}{3}; -\xi\right), \end{aligned} \tag{D 6}$$

while the coefficients, c_m, are given by Tulchinsky & Gat (2015),

$$c_m = \frac{(-1)^m}{12\pi \cdot 2^{2m}} \frac{\Gamma\left(\dfrac{m+1}{3}\right)}{\Gamma(m+1)^2}. \tag{D 7}$$

Taking the indefinite time integral of (D 6) (with the position-dependent integration function set to zero), we end up with the following expression for the transient

solution due to Heaviside actuation:

$$\begin{aligned}\eta_H(\boldsymbol{r},t) \;=\; & -\frac{\Gamma\left(-\frac{2}{3}\right)}{6}t^{2/3}\,{}_1F_5\left(-\frac{2}{3};\frac{1}{3},\frac{1}{3},\frac{2}{3},\frac{2}{3},1;-\xi\right)\\ & +\frac{\Gamma\left(-\frac{1}{3}\right)}{24}t^{1/3}\,{}_1F_5\left(-\frac{1}{3};\frac{2}{3},\frac{2}{3},1,\frac{4}{3},\frac{4}{3};-\xi\right)\\ & +\frac{\Gamma\left(\frac{4}{3}\right)^2\Gamma\left(\frac{5}{3}\right)^2}{384}r^4G^{2,0}_{1,6}\left(\begin{matrix}1\\0,0,-\frac{2}{3},-\frac{2}{3},-\frac{1}{3},-\frac{1}{3}\end{matrix}\middle|\,\xi\right),\end{aligned}\tag{D 8}$$

where ξ is the dimensionless variable given by (5.4). Integrating the expression (D 3) for η_D term by term (which is allowed due to uniform series convergence for $t>0$), or alternatively expanding (D 8), yields the following series representation of η_H:

$$\eta_H(\boldsymbol{r},t)=-t^{2/3}\sum_{m=0}^{\infty}\frac{3c_m}{1+m}\left(\frac{r^2}{t^{1/3}}\right)^m.\tag{D 9}$$

Figure 9 presents η_H solution, given by (D 8), at different times.

For the 1D case, the corresponding expression for the 1D Green's function is given by

$$\begin{aligned}\eta_D(x,t) \;=\; & -\frac{\Gamma\left(\frac{7}{6}\right)}{t^{1/6}}\,{}_0F_4\left(\frac{1}{3};\frac{1}{2},\frac{2}{3},\frac{5}{6};-\xi\right)-\frac{r^2\sqrt{\pi/t}}{12}\,{}_0F_4\left(\frac{2}{3};\frac{5}{6},\frac{7}{6},\frac{4}{3};-\xi\right)\\ & -\frac{r^4\Gamma\left(-\frac{1}{6}\right)}{864t^{5/6}}\,{}_0F_4\left(\frac{7}{6};\frac{4}{3},\frac{3}{2},\frac{5}{3};-\xi\right),\end{aligned}\tag{D 10}$$

while the transient solution due to Heaviside actuation in 1D is given by

$$\begin{aligned}\eta_H(x,t) \;=\; & -\frac{t^{5/6}\Gamma\left(-\frac{5}{6}\right)\Gamma\left(\frac{7}{6}\right)}{\Gamma\left(\frac{1}{6}\right)}\,{}_1F_5\left(-\frac{5}{6};\frac{1}{6},\frac{1}{3},\frac{1}{2},\frac{2}{3},\frac{5}{6};-\xi\right)\\ & -\frac{r^4t^{1/6}\Gamma\left(-\frac{1}{6}\right)}{144}\,{}_1F_5\left(-\frac{1}{6};\frac{5}{6},\frac{7}{6},\frac{4}{3},\frac{3}{2},\frac{5}{3};-\xi\right)\\ & -\frac{r^2t^{1/2}\sqrt{\pi}}{6}\,{}_1F_5\left(-\frac{1}{2};\frac{1}{2},\frac{2}{3},\frac{5}{6},\frac{7}{6},\frac{4}{3};-\xi\right).\end{aligned}\tag{D 11}$$

It is worth mentioning that since the Green's functions we found are all singular at $t=0$, difficulties are posed in constructing solutions for sources distributed along successive time moments. Specifically, direct solution of an equation with a time-dependent source, $\partial\eta_f/\partial t-\nabla^6\eta_f=f(\boldsymbol{r},t)$, expressed through convolution of η_D and f (a.k.a. Duhamel's principle), requires some regularization scheme, which is not discussed in this work. Nevertheless, it is straightforward to create solutions by performing spatial integration of sources, acting at a given time moment.

D.2. *Transient deformation due to a time decaying source*

Consider the resultant deformation due to a spatially localized signal, multiplied by a time-dependent function of the type

$$\frac{\partial\eta}{\partial t}-\nabla^6\eta=\frac{\mathrm{e}^{-r^2}}{1+t^b},\tag{D 12}$$

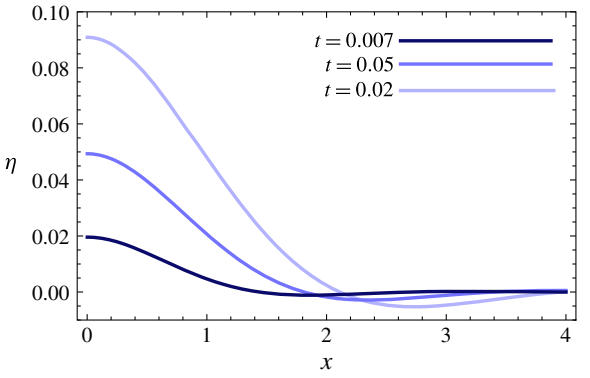

FIGURE 9. (Colour online) Analytical results presenting the 2D deformation under sudden actuation (Heaviside function), described by (D 8), at different times.

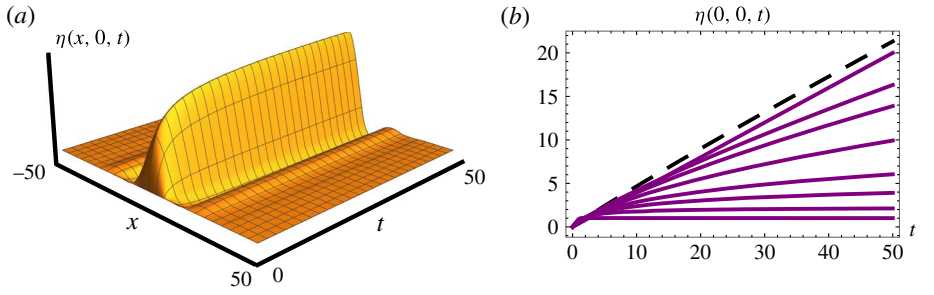

FIGURE 10. (Colour online) Numerical results showing the solution of (D 12), where the parameter b determines the temporal decay rate of the source and is allowed to acquire a set of values. (a) Deformation above the x–t plane for $y = 0$ and $b = 1.5$. (b) The time behaviour of the origin, for the following values: $b = 1/10,\ 1/4,\ 1/3,\ 1/2,\ 3/4,\ 1,\ 3/2,\ 10$. Lower values of b correspond to curves that lie closer to the dashed line $2t/5$. As $t \to \infty$, all solutions tend to zero. Nevertheless, prior to achieving this limit, the solution may violate the initial assumption of small deformation.

where b is a parameter. Figure 10 presents a numerical investigation of the solutions to (D 12), showing the maximal deformation at the origin as a function of time, for different values of the parameter b. The solutions show that when the actuation source does not decay rapidly enough, the maximal deformation grows and can eventually bring the solution out of the small-deformation regime. Of course, in practice there are plenty of stabilizing mechanisms such as physical walls and the liquid's own weight, which impose a restoring force on the elastic plate and may prevent the diverging behaviour (investigation of such models lies beyond the scope of the current study). Even without these mechanisms, for a sufficiently long time, the deformation in all cases examined decays to zero.

Appendix E. Deformation due to time-dependent actuation in a disk

In § 5, we determined the deformation due to harmonic actuation in 1D. In this appendix, we prove that the deformation due to harmonic actuation in a disk must take the form of a dipole.

Assume that we have solved the differential equation $L[\eta] = f(t)\delta(\boldsymbol{r})$, where L is some differential operator and f is some function of time argument. Similarly to our discussion near (C 2), the corresponding solution to the equation $L[\eta_R] = f(t)\cos(\varphi)\delta(r - R)$ is obtained by the following line integral along a circle of radius R:

$$\begin{aligned}\eta_R(r,\varphi) &= \int_0^{2\pi} \mathrm{d}\varphi'\, \eta(R^2 + r^2 - 2Rr\cos(\varphi - \varphi'))\cos(\varphi') \\ &= \sum_{m=0}^{\infty} c_m \int_0^{2\pi} \mathrm{d}\tilde{\varphi}(R^2 + r^2 - 2Rr\cos(\tilde{\varphi}))^m(\cos(\tilde{\varphi})\cos(\varphi) - \sin(\tilde{\varphi})\sin(\varphi)).\end{aligned} \tag{E 1}$$

In the second line of (E 1), we have transformed to the summation dummy variable $\tilde{\varphi}$ via $\tilde{\varphi} = \varphi - \varphi'$ and assumed that the function η admits a series expansion $\eta(r,t) = \sum_{m=0}^{\infty} c_m(t)r^m$. Integration term by term leads to

$$\begin{aligned}\eta_R(r,\varphi) &= \cos\varphi \sum_{m=0}^{\infty} c_m(t) \frac{\sqrt{\pi}}{\mathrm{i}rR(r^2 - R^2)} \frac{\Gamma(2+m)}{\Gamma\left(\frac{3}{2}+m\right)} \\ &\quad \times \left[\frac{r^2+R^2}{1+m}\left[(r-R)^{2+2m}\,{}_1F_2\left(\frac{1}{2}, 1+m, \frac{3}{2}+m; -\left(\frac{r-R}{r+R}\right)^2\right)\right.\right. \\ &\quad \left.\left. + (r+R)^{2+2m}\,{}_1F_2\left(\frac{1}{2}, 1+m, \frac{3}{2}+m; -\left(\frac{r+R}{r-R}\right)^2\right)\right] \right. \\ &\quad \left. + \frac{2}{3+2m}\left[(r+R)^{4+2m}\,{}_1F_2\left(\frac{1}{2}, 2+m, \frac{5}{2}+m; -\left(\frac{r+R}{r-R}\right)^2\right)\right.\right. \\ &\quad \left.\left. - (r-R)^{4+2m}\,{}_1F_2\left(\frac{1}{2}, 2+m, \frac{5}{2}+m; -\left(\frac{r-R}{r+R}\right)^2\right)\right]\right],\end{aligned} \tag{E 2}$$

which proves that the angular dependence of time-dependent actuation in a disk must be that of a dipole, and also provides a method to obtain the solution in terms of a series expansion, once the coefficients $c_m(t)$ are known. For a particular case of 2D harmonic actuation, the coefficients can be found by expanding the solution (5.10) into a Taylor series around the origin.

REFERENCES

AJDARI, A. 1995 Electro-osmosis on inhomogeneously charged surfaces. *Phys. Rev. Lett.* **75** (4), 755–759.

AJDARI, A. 1996 Generation of transverse fluid currents and forces by an electric field: electro-osmosis on charge-modulated and undulated surfaces. *Phys. Rev.* E **53** (5), 4996.

AL-HOUSSEINY, T. T., CHRISTOV, I. C. & STONE, H. A. 2013 Two-phase fluid displacement and interfacial instabilities under elastic membranes. *Phys. Rev. Lett.* **111** (3), 034502.

BAUDRY, J., CHARLAIX, E., TONCK, A. & MAZUYER, D. 2001 Experimental evidence for a large slip effect at a nonwetting fluid–solid interface. *Langmuir* **17** (17), 5232–5236.

BAZANT, M. Z., KILIC, M. S., STOREY, B. D. & AJDARI, A. 2009 Nonlinear electrokinetics at large voltages. *New J. Phys.* **11** (7), 075016.

BOYKO, E., RUBIN, S., GAT, A. D. & BERCOVICI, M. 2015 Flow patterning in Hele-Shaw configurations using non-uniform electro-osmotic slip. *Phys. Fluids* **27** (10), 102001.

BROTHERTON, C. M. & DAVIS, R. H. 2004 Electroosmotic flow in channels with step changes in zeta potential and cross section. *J. Colloid Interface Sci.* **270** (1), 242–246.

CHENG, Q., SUN, Z., MEININGER, G. A. & ALMASRI, M. 2010 Note: mechanical study of micromachined polydimethylsiloxane elastic microposts. *Rev. Sci. Instrum.* **81** (10), 106104.

CHRONIS, N., LIU, L. L., JEONG, K.-H. & LEE, L. P. 2003 Tunable liquid-filled microlens array integrated with microfluidic network. *Opt. Express* **11** (11), 2370–2378.

FEUILLEBOIS, F., BAZANT, M. Z. & VINOGRADOVA, O. I. 2009 Effective slip over superhydrophobic surfaces in thin channels. *Phys. Rev. Lett.* **102** (2), 026001.

GABOR, D. 1946 Theory of communication. Part 1: the analysis of information. *J. Inst. Electr. Engrs: Radio Commun. Engng* **93** (26), 429–441.

HOSOI, A. E. & MAHADEVAN, L. 2004 Peeling, healing, and bursting in a lubricated elastic sheet. *Phys. Rev. Lett.* **93** (13), 137802.

HUNTER, R. J. 2001 *Foundations of Colloid Science*. Oxford University Press.

KHAIR, A. S. & SQUIRES, T. M. 2008 Surprising consequences of ion conservation in electro-osmosis over a surface charge discontinuity. *J. Fluid Mech.* **615**, 323–334.

LANDAU, L. D., BELL, J. S., KEARSLEY, M. J., PITAEVSKII, L. P., LIFSHITZ, E. M. & SYKES, J. B. 1984 *Electrodynamics of Continuous Media*, vol. 8. Elsevier.

LANDAU, L. D. & LIFSHITZ, E. M. 1986 Theory of elasticity. *Course of Theoretical Physics* **3**, 109.

LISTER, J. R., PENG, G. G. & NEUFELD, J. A. 2013 Viscous control of peeling an elastic sheet by bending and pulling. *Phys. Rev. Lett.* **111** (15), 154501.

MICHAUT, C. 2011 Dynamics of magmatic intrusions in the upper crust: theory and applications to laccoliths on Earth and the Moon. *J. Geophys. Res.* **116** (B5), B05205.

MINOR, M., VAN DER LINDE, A. J., VAN LEEUWEN, H. P. & LYKLEMA, J. 1997 Dynamic aspects of electrophoresis and electroosmosis: a new fast method for measuring particle mobilities. *J. Colloid Interface Sci.* **189** (2), 370–375.

MORAES, C., LABUZ, J. M., SHAO, Y., FU, J. & TAKAYAMA, S. 2015 Supersoft lithography: candy-based fabrication of soft silicone microstructures. *Lab on a Chip* **15** (18), 3760–3765.

OLVER, F. W. J. 2010 *NIST Handbook of Mathematical Functions*. Cambridge University Press.

PANTON, R. L. 2006 *Incompressible Flow*. Wiley.

PENG, G. G., PIHLER-PUZOVIĆ, D., JUEL, A., HEIL, M. & LISTER, J. R. 2015 Displacement flows under elastic membranes. Part 2. Analysis of interfacial effects. *J. Fluid Mech.* **784**, 512–547.

PIHLER-PUZOVIĆ, D., ILLIEN, P., HEIL, M. & JUEL, A. 2012 Suppression of complex fingerlike patterns at the interface between air and a viscous fluid by elastic membranes. *Phys. Rev. Lett.* **108** (7), 074502.

PIHLER-PUZOVIĆ, D., JUEL, A., PENG, G. G., LISTER, J. R. & HEIL, M. 2015 Displacement flows under elastic membranes. Part 1. Experiments and direct numerical simulations. *J. Fluid Mech.* **784**, 487–511.

TRINH, P. H., WILSON, S. K. & STONE, H. A. 2014 An elastic plate on a thin viscous film. arXiv:1410.8558.

TRIVEDI, D., RAHN, C. D., KIER, W. M. & WALKER, I. D. 2008 Soft robotics: biological inspiration, state of the art, and future research. *Appl. Bionics Biomech.* **5** (3), 99–117.

TULCHINSKY, A. & GAT, A. D. 2015 Transient dynamics of elastic Hele-Shaw cell due to external forces with application to impulse mitigation. *J. Fluid Mech.* **800**, 517–530.

UNGER, M. A., CHOU, H. P., THORSEN, T., SCHERER, A. & QUAKE, S. R. 2000 Monolithic microfabricated valves and pumps by multilayer soft lithography. *Science* **288** (5463), 113–116.

VAN DER WOUDEN, E. J., HEUSER, T., HERMES, D. C., OOSTERBROEK, R. E., GARDENIERS, J. G. E. & VAN DEN BERG, A. 2005 Field-effect control of electro-osmotic flow in microfluidic networks. *Colloids Surf.* A **267** (1), 110–116.

VINOGRADOVA, O. I. 1999 Slippage of water over hydrophobic surfaces. *Intl J. Miner. Process.* **56** (1), 31–60.

YARIV, E. 2004 Electro-osmotic flow near a surface charge discontinuity. *J. Fluid Mech.* **521**, 181–189.